Nanoscale

PAPER

View Article Online
View Journal | View Issue

Cite this: *Nanoscale*, 2024, **16**, 12459

Neodymium niobate nanospheres on functionalized carbon nanofibers: a nanoengineering approach for highly sensitive vanillin detection†

I. Jenisha Daisy Priscillal and Sea-Fue Wang *

Vanillin (VAN), the primary aroma compound in vanilla, contributes significantly to sensory delight; however, its unrestrained presence poses notable health risks. In response to the demanding concern regarding food safety, researchers have directed their efforts towards the detection of VAN, seeking sustainable strategies for contamination prevention. A groundbreaking solution has emerged in the form of a novel sensing platform, whose core lies on a finely tuned electrode, crafted through the incorporation of nano-sized $NdNbO_4$ spheres onto carbon nanofibers (CNFs). This incorporation serves to augment the capabilities of a glassy carbon electrode (GCE), transforming it into a highly sensitive detector primed for vanillin detection. The $NdNbO_4$/f-CNF nanocomposite embodies a paradigm of synergistic collaboration, wherein the nonlinear cumulative effects of synergism and quantum confinement impart exceptional performance characteristics. Notably, the sensor achieves a low detection limit of 6.3 nmol L^{-1}, indicative of its remarkable sensitivity of 2.3 μA μ(mol $L^{-1})^{-1}$ cm^{-2} and precision of 1.519 and 4.72%. Moreover, the sensor boasts a wide linear range spanning from 0.001 to 63.101 μmol L^{-1}. These attributes, coupled with its discerning selectivity and robust stability, underscore its efficacy as a versatile tool for vanillin detection. Indeed, its successful deployment in monitoring food samples underscores its applicability across diverse culinary contexts, further cementing its status as a pivotal asset in safeguarding food quality and consumer well-being.

Received 4th February 2024,
Accepted 26th May 2024

DOI: 10.1039/d4nr00521j

rsc.li/nanoscale

1. Introduction

In the contemporary culinary landscape, the allure of food hinges greatly on the nuanced play of flavors, often augmented by the judicious use of flavor enhancers. Among these, vanilla reigns supreme, lending its distinctive essence to a plethora of everyday indulgences such as cookies and chocolates. Vanillin (VAN, 4-hydroxy-3-methoxy benzaldehyde) is a key aroma compound in vanilla associated with positive emotional experiences and possessing anti-epileptic and anti-anxiety effects.[1] Despite over 12 000 tons of annual production, less than 1% comes from natural vanilla orchids, with the majority synthesized chemically.[2] Controlled vanillin intake offers antioxidant, antidepressant, anticancer, and anti-inflammatory benefits, particularly aiding anemic patients.[3–5] However, excessive consumption can lead to liver, spleen, and kidney damage, as well as health issues like nausea, headaches, vomiting, and allergic reactions.[3,6] To address these concerns, the China National Food Safety Standard and Joint FAO/WHO Expert Committee on Food Additive (JECFA) has set strict guidelines for vanillin consumption,[7,8] emphasizing the need for rigorous monitoring of vanillin levels in food products.

Department of Materials and Mineral Resources Engineering, National Taipei University of Technology, No. 1, Sec. 3, Chung-Hsiao East Rd., Taipei 106, Taiwan. E-mail: sfwang@ntut.edu.tw

† Electronic supplementary information (ESI) available. See DOI: https://doi.org/10.1039/d4nr00521j

I. Jenisha Daisy Priscillal is currently doing her Ph.D. in Materials and Mineral Resources Engineering at the National Taipei University of Technology, Taiwan. Her research is mainly focused on bimetal oxides and nano-heterostructured carbon composites for electrochemical sensors and supercapacitors. Email: jenishadaisyi@gmail.com

Sea-Fue Wang received his Ph.D. from the Pennsylvania State University and is currently serving as a distinguished professor in the Department of Materials and Mineral Resources Engineering at the National Taipei University of Technology. His works mainly focus on solid oxide fuel cells, electrochemical sensors, bioceramics, and lithium-ion batteries. Email: sfwang@ntut.edu.tw

In recent days, numerous procedures have been described for the detection of vanillin, including gas chromatography,[9] gas chromatography-mass spectrometry (GC-MS),[10] high-performance liquid chromatography,[11,12] liquid chromatography-mass spectrometry (LC-MS),[13] chemiluminescence,[14] capillary electrophoresis,[15] and colorimetry.[16] These existing methodologies necessitate a state-of-the-art lab environment, sophisticated instrumentation, tedious sample preparation, and a skilled operator for successful experimental execution.[16,17] These methods fall short in practical applications due to issues like non-repeatability and the inability to conduct on-site testing. Conversely, modern electrochemical sensors are designed for field deployment, addressing space and power constraints with cost-effective instrumentation.[18] The radical advancements in nanotechnology and nanoengineering have led to the discovery of eminent sensing platforms with a remarkable surface *versus* volume ratio.[19] Among the prevailing sensing techniques, the voltammetry approach is more beneficial as it is inherently fast, strongly sensitive, and highly selective and offers minimal detection and quantification limits.[20] The implementation of the aforementioned factors strongly depends on the electron transit, aspect ratio, potential window, and background current of the working electrode. A glassy carbon electrode (GCE) is chosen as the working electrode as it is a gas-impermeable conductive material resistive to erosion by chemicals. This electrode is capable of amplifying signals over a wide potential window ranging from +1.2 V to −0.8 V.[21] The current challenge relies on finding electroactive materials whose sensing characteristics might be readily altered to create sensors with cross-selectivity and good stability which is obligatory for the construction of novel voltammetric sensors.

Recent advancements have introduced various GCE modifiers, including lanthanum nickelate anchored carbon fibers,[22] CuO/NiO nanocomposites,[23] MoS_2 nanosheets on g-C3N4 nanotubes,[24] and $LaCoO_3$ with carbon nanofibers,[25] for sensitive vanillin detection. Drawing inspiration from this literature, carbon nanofibers (CNFs) have been selected for exploration as an electrode modifier. The cone helix structure of CNFs undergoes structural transformation under vigorous conditions to form a stacked cone structure with a high aspect ratio. In order to activate the edge planes of CNFs, acid functionalization is carried out which introduces oxygen functionalities at the periphery of the carbon backbone which increases the surface-active group-to-volume ratio, thereby acting as an immobilization matrix.[26]

On the other hand, in the modern era, rare earth metal oxides (REMOs) are considered as prime candidates for surface modification due to their noteworthy catalytic behavior, rapid oxygen ion mobility, effective charge transfer, and high surface basicity.[27] Rare earth niobates, a unique subset of REMOs, present challenges in their exploration as electrode materials due to their complex structure and synthesis methods. They comprise perovskite-like slabs with the formula ABO_4, where A represents an f-block cation (*e.g.*, Nd^{3+}) and B typically refers to a tiny transition metal cation, such as niobium in its 5+ oxidation state. The complexity arises primarily from the potential coordination of the niobium cation, leading to reversible ferroelastic phase transitions and lattice deformations, resulting in significant macroscopic stresses within the lattice.[28] The known niobates, with the exception of scheelites and fergusonites, are dominated by pentavalent Nb atoms in octahedral coordination. These niobates are recognized as fundamental mysteries of crystal chemistry because Nb^{5+} only exhibits tetrahedral coordination with oxygen and the interatomic gap between Nb–O and Nb–O in Nb_2O_5 is higher.[29] This study aims to develop a simple hydrothermal technique that uses superheated aqueous solution processing under high pressure and temperature conditions to dissolve and recrystallize (recover) materials that are generally insoluble under ordinary circumstances.[30] The goal is to produce the pure phase of $NdNbO_4$ with valuable physiognomies.

To enable $NdNbO_4$ nanocrystalites to function as an efficient electrocatalyst, a CNF is used as an immobilization matrix. The nanocomposite prepared operates as a renowned transducer due to the cumulative effects of the individual constituents acquired through the formation of a hybrid heterojunction that enhances the conduits for electrochemical signal transmission. The $NdNbO_4$/f-CNF nanocomposite is described here as an active electrode modification for the very sensitive detection of VAN. Through crystallographic, spectroscopic, and microscopic techniques, the produced nanocomposite was carefully studied. Additionally, the electrochemical parameters have been adjusted, and by expanding the experiments to food sample analysis, the practicability was examined.

2. Experimental section

2.1. Chemicals and reagents

Neodymium nitrate ($Nd(NO_3)_3 \geq 99\%$ purity), niobium pentachloride ($NbCl_5 \geq 99\%$ purity), hydrogen peroxide (H_2O_2), and urea (CH_4N_2O) were purchased from Sigma Aldrich and carbon nanofibers (CNFs) were purchased from Rur-Grapheneox Company. All other necessary reagents and the abovementioned chemicals have been used without further refinement. The preparation of phosphate-buffered saline (PBS, 0.1 M) involved the utilization of sodium phosphate dibasic (Na_2HPO_4) and sodium dihydrogen phosphate (NaH_2PO_4). To adjust the pH of the buffer solution, 1 N HCl and 0.1 M NaOH solutions were employed. 0.5 mM ferricyanide $[Fe(CN)_6]^{3-/4-}$ solution was prepared by adding potassium ferrocyanide ($K_4[Fe(CN)_6]\cdot 3H_2O$) and potassium ferricyanide ($K_3[Fe(CN)_6]$) in 0.1 M KCl. All the experiments used ultrapure fresh water obtained from a Millipore water purification system (Milli-Q, specific resistivity > 18 MΩ cm, S.A., Molsheim, France).

2.2. Instrumentation

Phase configurational analysis was carried out by X-ray diffraction (XRD) using the D2 Phaser XRD instrument. The chemical composition of the materials was quantitatively examined

using X-ray photoelectron spectroscopy ESCA/Auger Laboratory (National Taiwan University, Taiwan). Structural morphology and elemental composition were investigated with the aid of energy-dispersive X-ray spectroscopy (EDX) incorporated with field-emission scanning electron microscopy (FESEM, JEOL JSM-7100F). Detailed crystallite information of the as-prepared nanocomposite was analyzed using high-resolution transmission electron microscopy (HRTEM) (H-7600, Hitachi, Japan) operating at 200 kV, alongside EDX (HORIBA EMAX XACT) spectroscopy.

2.3. Synthesis of $NdNbO_4$

In a typical synthetic procedure, a 50 mL homogeneous solution containing 0.05 M niobium pentachloride ($NbCl_5$) was prepared and constantly maintained in an ice bath at 10 °C. While under the cold conditions, 15 mL of hydrogen peroxide was added dropwise to the prepared solution with continuous agitation. Subsequently, excess ammonia solution was slowly added to the reaction mixture until saturation, resulting in the formation of an ammonium tetra peroxo niobate complex ($(NH_4)_3[Nb(O_2)_4]$). Following the removal of the ice bath, 50 mL of 0.05 M $Nd(NO_3)_3{\cdot}6H_2O$ solution was introduced and stirring was continued for 20 minutes. Eventually, 0.1 M urea was added to the reaction mixture, which was then transferred to a Teflon-lined autoclave and maintained under hydrothermal conditions for 24 hours at 180 °C. The suspension obtained post-hydrothermal processing was subjected to centrifugation to obtain the precipitate, which was then washed multiple times to eliminate impurities and achieve the desired $NdNbO_4$ nanocryslalite.

The formation of a peroxocomplex intermediate leads to the release of a considerable amount of Nb^{5+} ions in the reaction medium. Simultaneously, urea undergoes conversion to ammonia and isocyanic acid, which further decomposes into CO_2 and NH_3. Upon the addition of $Nd(NO_3)_3$ to the mixture, the reaction tends to promote the formation of neodymium niobium hydroxide carbonate. Under the influence of high temperature and pressure, this compound eliminates CO_2 and H_2O from carbonates and hydroxide moieties to precipitate out $NdNbO_4$.

2.4. Functionalization of the CNF

Edge site activation of the pristine CNF was accomplished *via* acid functionalization. This process employs an oxidant consisting of concentrated nitric acid and concentrated sulfuric acid in a 1 : 3 volume ratio. The CNF was dispersed within the acidic mixture, resulting in the formation of a dense suspension, which was continuously stirred magnetically for 1 hour at 60 °C. Following evaporation, a thick black slurry was obtained. This slurry was then dispersed in DI water and subjected to centrifugation to eliminate the acidic mixture. This cycle was repeated multiple times, with the pH being monitored after each iteration using a pH meter. Once the slurry reaches a neutral pH, the residues were washed with ethanol and left to dry overnight. The resulting functionalized CNF exhibits enhanced solubility and electrical conductivity due to the introduction of oxygen functionalities.

2.5. Preparation of the $NdNbO_4$/f-CNF composite

To retain the structural and morphological integrity, hydrothermally synthesized $NdNbO_4$ nanoparticles were integrated into the network of functionalized CNF *via* sonochemical techniques. The weight ratio (1 : 1) of $NdNbO_4$ to f-CNF was accurately measured and dispersed in deionized water, leading to the formation of a colloidal solution. Upon centrifugation, the nanocomposite residues were effectively separated. Subsequently, the residues were dried, labeled based on the specific ratio, and then used for subsequent comprehensive characterization. This systematic preparation is demonstrated in Fig. 1.

2.6. Fabrication of the electrode

Utilizing suitable electrode modifiers, drop casting emerges as a rapid and versatile technique for the construction of modified electrodes. Prior to the surface modification process, 3 mg of the as-prepared electrode modifier, $NdNbO_4$/f-CNF, was dispersed in 1 mL of deionized water through 15 minutes of sonication. Subsequently, a GCE was polished using alumina powder (0.05 μm) to eliminate any adsorbed impurities. From the suspension containing the desired modifier, 6 mg μL^{-1} was carefully pipetted and cast onto the surface of the GCE. The droplet, upon contact with the electrode surface, experienced a surface tension gradient, resulting in an outward convective flow known as Marangoni flow influenced by interfacial forces. As the inward Marangoni flow velocity surpassed the outward capillary flow, the solute concentrated at the center, facilitating the adsorption of the desired particles and enabling surface modification. Following this, the coated electrodes were dried at 60 °C for 3 minutes and then prepared for electrochemical experimentation.

2.7. Electrochemical characterization

2.7.1. Electrochemical impedance spectroscopy (EIS). EIS is a steady-state method that functions *via* small signal analysis, enabling the assessment of signal relaxations over a wide range of frequencies, from below one MHz to over 1 MHz, utilizing a potentiostat. The impedimetric analysis of all the modified GCEs was conducted using the Ω-metrohm autolab (AUT51770, 100–240 V~ 75VA50/60 Hz) in a 5 mM $[Fe(CN)_6]^{3-/4-}$ solution within 0.1 M KCl as the electrolyte solution. A simplified Randel's equivalent circuit was utilized to represent electrified interface parameters, including the solution resistance, double-layer capacitance, Warburg impedance, and charge transfer resistance, as depicted in Fig. S1.† According to the proposed equivalent circuit, the impedance at a specific frequency is portrayed as a Nyquist plot, where the real part was plotted along the *X*-axis and the imaginary part was plotted along the *Y*-axis. The interface resistance was determined by reading the real axis value at the high-frequency value, while the variation in the slope's magnitude is illustrated at low frequencies.

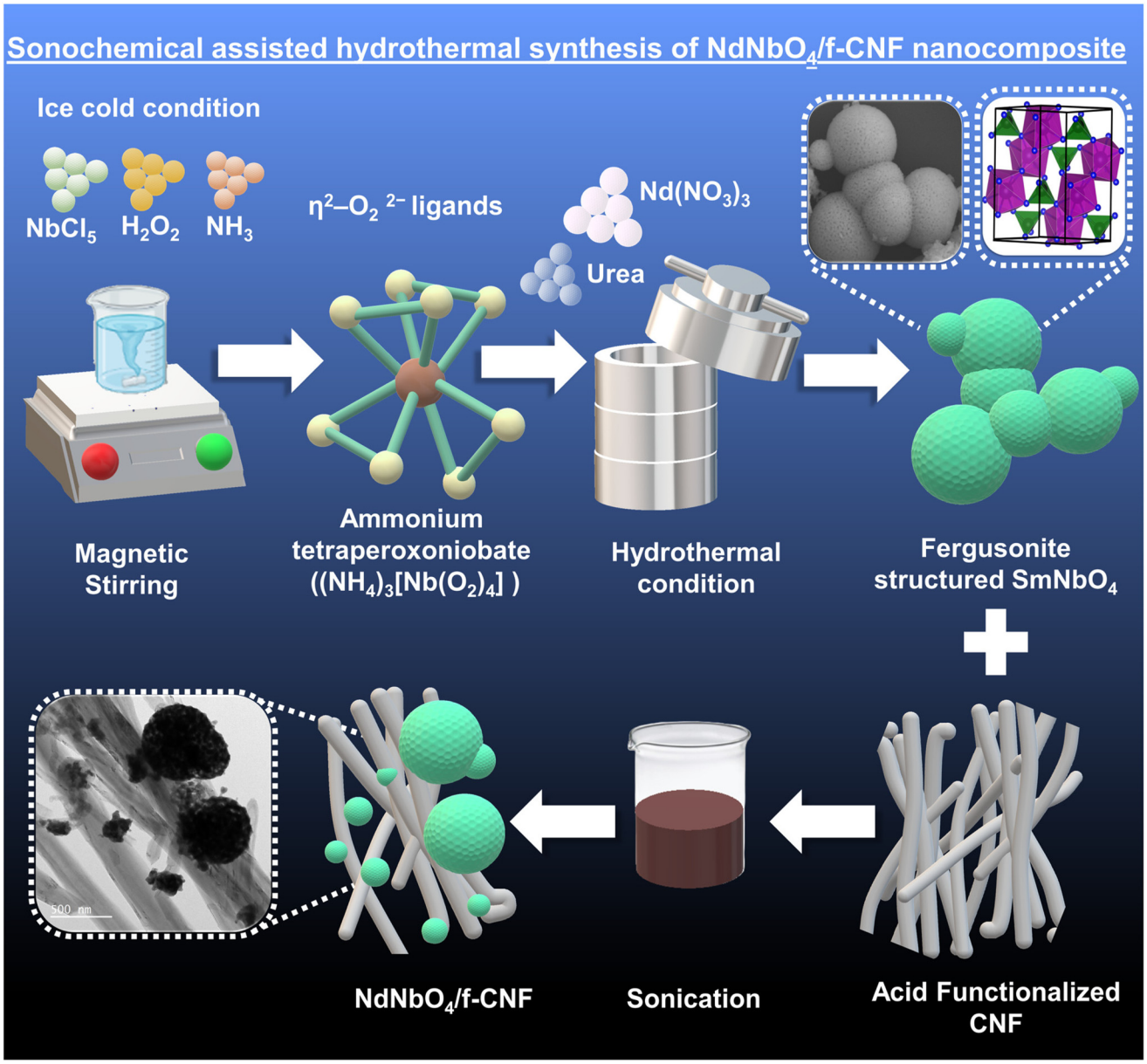

Fig. 1 Schematic representation of the synthesis of the $NdNbO_4$ reinforced f-CNF nanocomposite.

2.7.2. Cyclic voltammetry (CV). CV serves as an electrochemically potentiodynamic technique in which the potential of the working electrode is systematically ramped linearly over electron flow. Utilizing the CHI 1205A electrocatalytic workstation, CV measurements were effectively conducted within a three-electrode cell setup, employing a GCE as the working electrode, an Ag/AgCl electrode as the reference electrode, and a platinum wire as the counter electrode. During the experiment, the potential was measured between the working electrode and the reference electrode, while the current was measured between the working electrode and the counter electrode. The rate at which the voltage changes over time during each phase is commonly referred to as the scan rate ($mV\ s^{-1}$).

2.7.3. Calibration curve and linearity. The direct correlation between the redox peak currents and various electrochemical parameters, including the analyte concentration, electrolyte pH, and scan rates, among others, is meticulously illustrated through the construction of graphs in adherence to Beer's law and the linear regression model. The degree of linearity within each plot was evaluated according to the IUPAC standard, where a value nearing 1 signifies a robust fit. Moreover, the linearity of the data was rigorously verified through the computation of the lack-of-fit and F-distribution based on the linear regression model (LRM).

2.7.4. Precision in the electrochemical assay. The accuracy and reliability of the voltammetry assay were thoroughly assessed across various concentrations of the analyte, diverse

electrode modifications, and through multiple iterations. The determination of the relative standard deviation (RSD) for each of these parameters was conducted using the following eqn (1):

$$\mathrm{RSD} = \frac{100 \times \mathrm{SD}}{\text{mean of determination}} \quad (1)$$

2.7.5. Accuracy of detection. Differential Pulse Voltammetry (DPV) stands as an advanced voltammetry technique that effectively diminishes faradaic currents through the implementation of small potential perturbations. DPV's distinctive capability lies in its ability to offer enhanced selectivity for observing various redox processes in contrast to conventional voltammetry. Through the utilization of the LRM, the linear relationship between the concentration of the analyte and the redox peak current was carefully plotted, aiming for an R^2 value that approaches 1. Furthermore, the limit of detection (LOD) and the limit of quantification (LOQ) were estimated using eqn (2) and (3), providing an essential measure of the smallest concentration of the analyte that can be reliably detected.

$$\mathrm{LOD} = \frac{3\,\mathrm{SD}}{m} \quad (2)$$

$$\mathrm{LOQ} = \frac{10\,\mathrm{SD}}{m} \quad (3)$$

Here, SD is the standard deviation obtained from three measurements of the blank signal and m is the analytical sensitivity represented by the slope of the calibration plot.

2.8. Real sample preparation

For the real sample analysis, a chocolate bar and a milkshake were specifically chosen. A commercially available packet of each was obtained from local supermarkets in Taipei, Taiwan, and processed as real samples for the study.

I. About 0.50 g of the chocolate bar was introduced into 20 mL of deionized water and heated to 60 °C in a water bath employing the double-boiling method to facilitate melting. Subsequently, the sample underwent centrifugation at 4000*g* force for 5 minutes, leading to the separation of the supernatant, which was then diluted in 0.1 M PBS for subsequent analysis.

II. Similarly, 1 mL of the milkshake was added to 5 mL of deionized water and further diluted in 10 mL of 0.1 M PBS, subsequently being directly utilized for the electrocatalytic evaluation of the prepared composite.

3. Results and discussion

3.1. Characterization of the $NdNbO_4$/f-CNF nanocomposite

3.1.1. Crystallographic analysis. Fig. 2(A) displays the X-ray diffractograms of both pure $NdNbO_4$ and the $NdNbO_4$/f-CNF nanocomposite. According to information sourced from the powder diffraction file (PDF) 00-013-0180, $NdNbO_4$ possesses a monoclinic crystal structure with a space group designated as $C2/c$. In the depicted crystal structure (refer to Fig. 2(B)), Nd^{3+} exhibits coordination in an 8-coordinate geometry, engaging with eight O^{2-} atoms. Conversely, Nb^{5+} forms bonds with six O^{2-} atoms, creating distorted edge-sharing NbO_6 tetrahedra. The crystal structure reveals two distinct O^{2-} sites: the first, with O^{2-} coordinated in a 3-coordinate geometry to two equivalent Nd^{3+} ions and one Nb^{5+} ion; the second, where O^{2-} is coordinated in a 4-coordinate geometry to two equivalent Nd^{3+} ions and two equivalent Nb^{5+} ions. The diffraction pattern of the $NdNbO_4$/f-CNF composite exhibits characteristic peaks of monoclinic $NdNbO_4$, along with a prominent peak at 26.5° attributed to the (002) graphitic plane of f-CNF. This confirms the successful formation of the nanocomposite, which encompasses phases of both $NdNbO_4$ and f-CNF.

The average crystallite size of $NdNbO_4$ was calculated using the Debye–Scherrer formula expressed as:

$$D = \frac{K\lambda}{\beta \cos\theta} \quad (4)$$

where D represents the average crystallite size, K is Scherrer's constant, λ denotes the wavelength (with a specific value of 0.1540 nm), β stands for the full-width half maximum (FWHM) of the diffraction peak, and θ signifies Bragg's diffraction angle. The Scherrer's constant, K, also known as the shape factor, plays a crucial role in converting the experimental data from X-ray diffraction studies into meaningful information about the size of the crystallites. With a precise calculation using eqn (4), the average crystallite size of $NdNbO_4$ is found to be 43.06 nm. This result provides valuable insights into the structural characteristics of $NdNbO_4$, shedding light on the dimensions of its crystalline constituents.[17]

3.1.2. Raman analysis. Fig. 2(C) displays the Raman spectra of $NdNbO_4$/f-CNF, revealing the presence of two bands within the nondegenerate symmetric range (700–1000 cm^{-1}). The monoclinic transformation of the structure identified in the $C2/c$ space group has 2 Nb atoms per unit cell at site symmetry $C3\sim$.[31] Consequently, the bands exhibit a split, manifesting as a weaker band at 790 cm^{-1} and a stronger one at 906 cm^{-1} due to the trigonal field at the Nb^{5+} site. In the frequency range of 90–280 cm^{-1}, the observed vibrations are predominantly attributed to the deformation of the Nb–O framework influenced by displacements of Nd cations. The O–Nb–O bending modes are notable at and below 480 cm^{-1}, exhibiting strong coupling with the Nd–O stretching and O–Nd–O bending modes at 320, 365, and 398 cm^{-1}.[32] Additionally, characteristic peaks at 1359 cm^{-1} and 1535 cm^{-1} correspond to the G and D bands of f-CNF. The G-band is ascribed to the in-plane stretching vibrations of sp^2 hybridized C–C bonds in chains or six-fold aromatic rings with E_{2g} symmetry. Simultaneously, the D-band arises from the symmetric vibrations of the A_{1g} breathing modes of sp^2 hybridized carbon structures in hexagonal aromatic rings. According to the symmetry forbidden rule, the D-band is inactive in a perfect graphitic structure but becomes active in the presence of disorder/defects in the resonance of sp^2 carbon in the graphitic skeleton.[33] These findings provide additional support for the successful formation of the $NdNbO_4$/f-CNF nanocomposite.

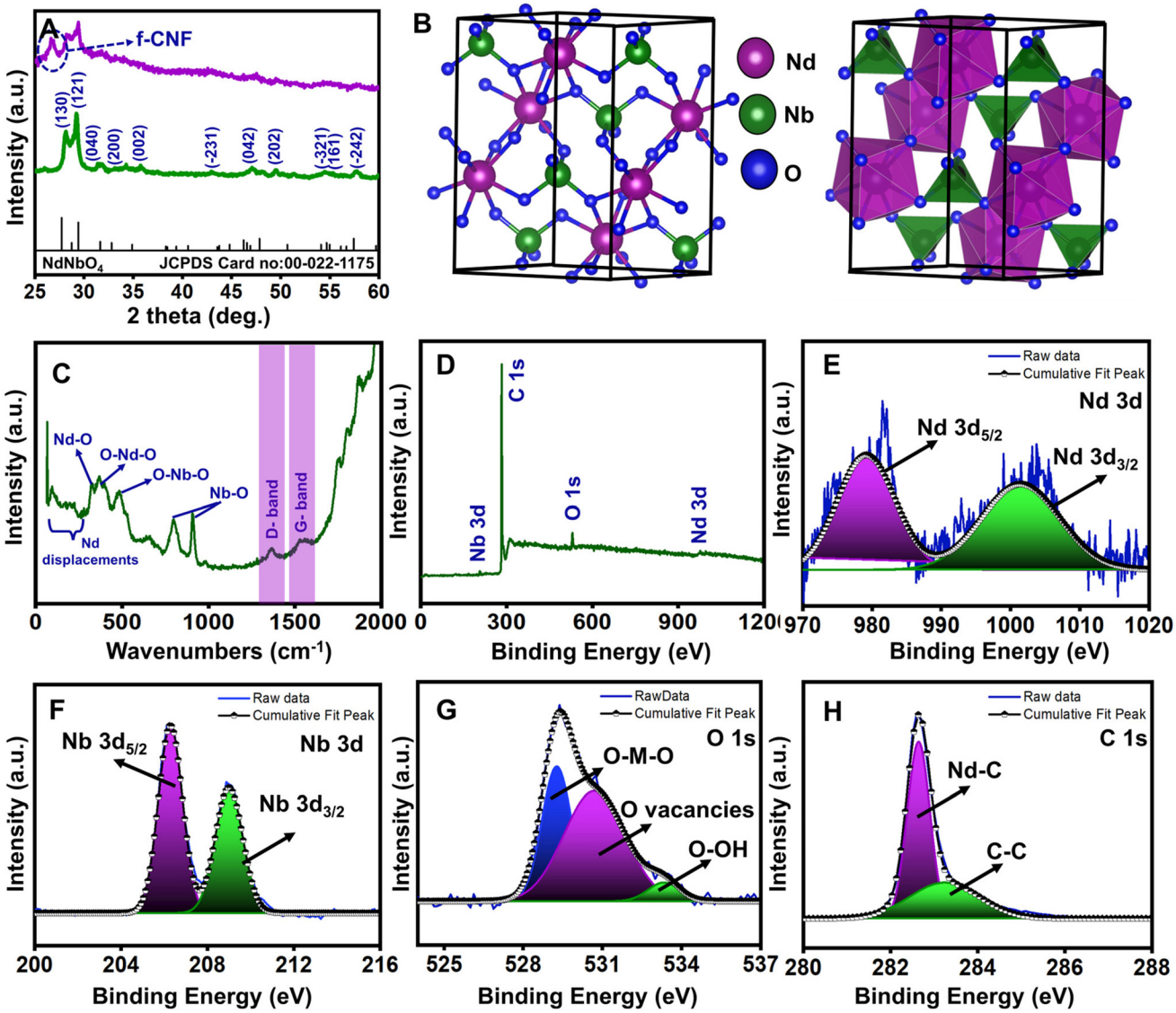

Fig. 2 (A) X-ray diffraction patterns of pure $NdNbO_4$ and the $NdNbO_4$/f-CNF nanocomposite; (B) crystal structure of $NdNbO_4$ nanocrystallites; (C) Raman spectra of the $NdNbO_4$/f-CNF nanocomposite; (D) XPS survey spectra of the $NdNbO_4$/f-CNF nanocomposite; and high-resolution XPS spectra of (E) Nd 3d, (F) Nb 3d, (G) O 1s and (H) C 1s.

3.1.3. Elemental analysis. X-ray photoelectron spectroscopy (XPS) serves as a valuable tool for probing the surface chemistry of nanocrystallites, allowing for the identification of elemental composition and the determination of oxidation states. The XPS survey spectrum, as depicted in Fig. 2(D), shows the presence of Nd, Nb, O, and C on the surface of the nanocomposite under investigation. In the Nd 3d core level spectrum (Fig. 2(E)), two discernible spin–orbit features are observed at binding energy (BE) values of 979.29 eV and 1001.5 eV, corresponding to the Nd $3d_{3/2}$ and Nd $3d_{5/2}$ components, respectively.[34] This observation points to the presence of Nd in the Nd^{3+} oxidation state. The energy difference between these peak spin–orbit values (22.29 eV) closely aligns with the literature reported value of 22.50 eV, validating the oxidation state assignment.[35–37] Similarly, the Nb 3d spectra (Fig. 2(F)) exhibit spin–orbit coupling peaks at 206.24 eV and 208.95 eV, attributed to Nb $3d_{3/2}$ and Nb $3d_{5/2}$, respectively, with an energy difference of 2.71 eV. This finding indicates the Nb^{5+} oxidation state.[38,39] Further analysis in Fig. 2(G) involves the deconvolution of the O 1s spectra, revealing three distinct peaks at 529.25 eV, 530.61 eV, and 533.31 eV. These peaks are associated with metal–oxygen bonds, oxygen vacancies, and O–OH bonds in oxygen functionalities introduced at the periphery of the carbon nanofiber (CNF). Lastly, the C 1s spectra (Fig. 2(H)) are characterized by two deconvoluted peaks. The peak at 283.2 eV is attributed to C–C linkages in the CNF.[40] Notably, an intense peak at 282.65 eV is assigned to a surface C–Nd species, showcasing the interaction of carbon with neodymium.[41] It is worth mentioning that similar peaks have been reported in other systems, such as C–Ti at 281.7 eV and

C–Pr at 282.4 eV, providing a reference for the interpretation of these carbon-related features.[41,42]

3.1.4. Morphological analysis. FESEM analysis was employed to examine the morphological characteristics of pristine f-CNF and $NdNbO_4$ nanocrystals. In Fig. 3(A), slender fibrils of f-CNF are illustrated, showcasing a randomly oriented structure without beads and a smooth surface. These fibrils have average diameters ranging from 5 to 100 nm. On the other hand, $NdNbO_4$ demonstrates a distinctive spherical morphology (Fig. 3(B and C)), a characteristic attributed to the

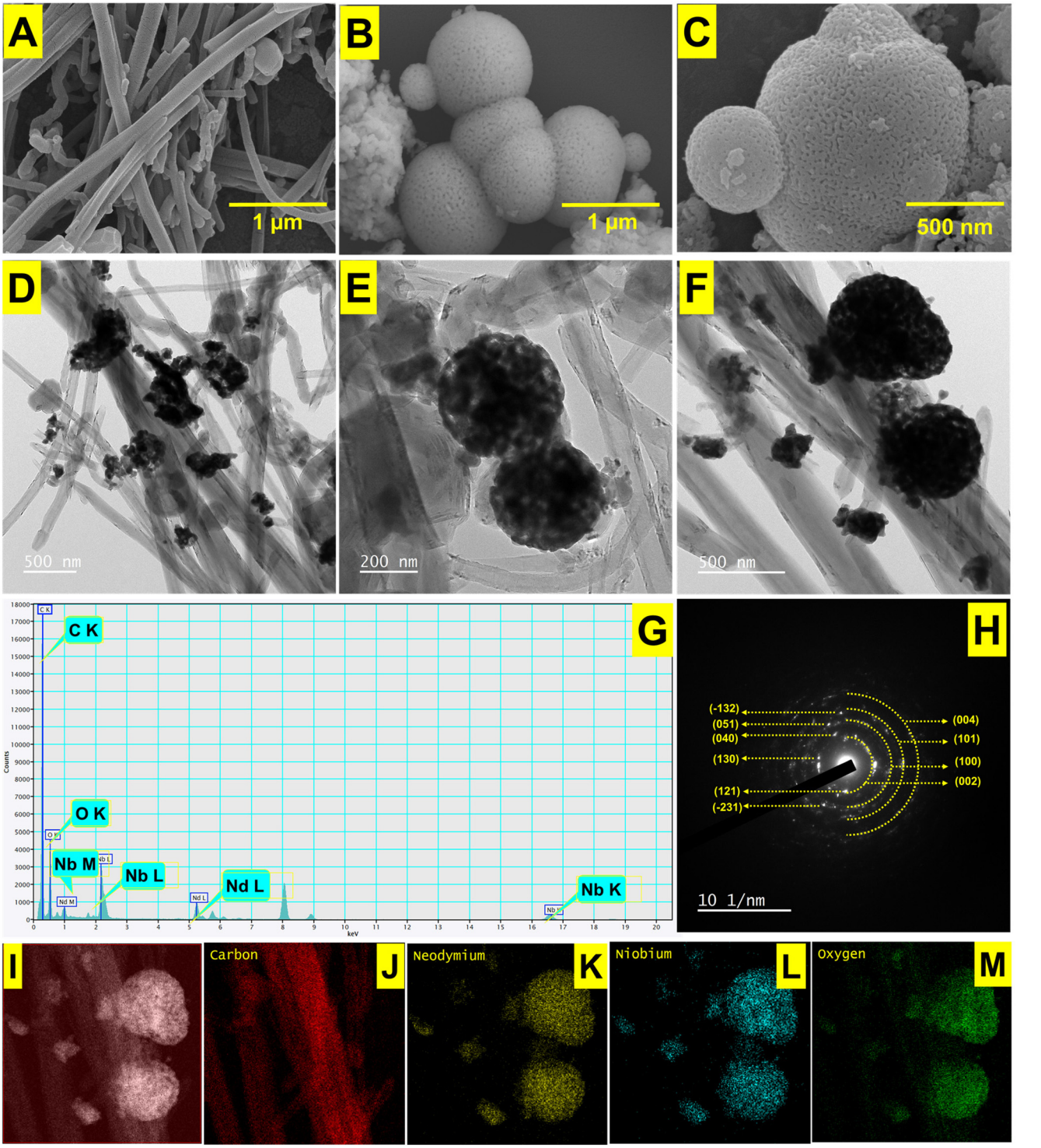

Fig. 3 FESEM micrographs of (A) f-CNF and (B and C) $NdNbO_4$; (D–F) TEM images, (G) EDX spectrum, (H) SAED pattern, and (I–M) elemental mapping of the $NdNbO_4$/f-CNF nanocomposite.

equilibrium between elevated pressure and controlled temperature within the reaction vessel. This combination facilitates the uniform dissolution of reactants and the nucleation of particles, influencing growth kinetics and ultimately giving rise to spherical shapes. The spherical morphology is a consequence of the tendency of particles to minimize surface energy, prompting them to adopt shapes that reduce their overall surface area. It is worth noting that the surface of these spheres is not perfectly smooth; instead, it exhibits irregularities.[43] This irregular surface structure contributes to an increased surface area, which, in turn, facilitates easy penetration of electrolytes during electrocatalytic reactions.[44] Furthermore, TEM was used to characterize the $NdNbO_4$/f-CNF nanocomposite and the respective micrographs are given in Fig. 3(D–F). The TEM images clearly represent the structural integration between the nanofibrous matrix and the spherical $NdNbO_4$ components within the composite material. The successful incorporation of $NdNbO_4$ into f-CNF is confirmed through EDX analysis, which validates the coexistence of Nd, Nb, O, and C through the corresponding peaks observed in the EDX spectrum depicted in Fig. 3(G). The SAED pattern presented in Fig. 3(H) exhibits concentric circles at *d*-spacing values of 3.3 Å, 2.12 Å, 2.02 Å, and 1.69 Å corresponding to the (002), (100), (101), and (004) graphitic planes of f-CNF. Additionally, bright spots in the pattern correspond to the (130), (121), (040), (−231), (051), and (−132) lattice planes of $NdNbO_4$ crystallites. The spatial distribution of individual constituents in the composite is clearly demonstrated by the EDX mapping shown in Fig. 3(I–M).

3.2. Electrocatalytic activity of the $NdNbO_4$/f-CNF nanocomposite

EIS operates by introducing a signal of predetermined amplitude as a stimulus superimposed on the DC signal of the electrochemical system. This signal was then applied across a wide range of frequencies, and the resulting response was measured. The impedance analysis of a cell, featuring four terminals and three electrodes in potentiostatic mode, involved the utilization of a redox probe. A sinusoidal voltage, overlaying a DC potential aligned with the standard electrochemical potential (E°) of the redox reaction, was employed for this measurement.

$$[Fe(CN)_6]^{3-} + e^- \leftrightarrow [Fe(CN)_6]^{4-} \quad (5)$$

In accordance with Randel's equivalent circuit (refer to Fig. S1†), the impedance (Z_F) of the faradaic process can be elucidated as a composite of the following two components:

$$z_F = R_{Ct} + Z_w \quad (6)$$

I. The charge-transfer resistance, denoted as R_{ct}, correlates with the rate of the heterogeneous redox reaction, assuming the non-adsorption of oxidizing and reducing species on the electrode surface. The Nyquist plots presented in Fig. S1† depict that the unmodified GCE exhibited a higher R_{ct} value (2128.61 Ω) compared to all other modified electrodes which indicates the necessity for electrode modification. Upon modification of the GCE with $NdNbO_4$ and f-CNF, the R_{ct} value significantly decreases to 655.84 and 149.67 Ω, respectively. This reduction is primarily attributed to the activation of the glassy carbon layer in the electrolyte through enhanced electron mobility provided by the electron-rich modifiers. Furthermore, the GCE modified with the $NdNbO_4$/f-CNF nanocomposite exhibits a further reduction in the R_{ct} value to 41.31 Ω. This reduction is ascribed to the formation of a hybrid heterojunction, facilitating rapid charge transportation between counterparts, along with improved electron transport at the electrified interface.

II. The Warburg impedance (Z_W) is defined as the resistance encountered in transporting redox species across the electrode surface in the context of semi-infinite linear diffusion. The Nyquist plot's linear segment reflects the Warburg impedance. In the case of the $NdNbO_4$/f-CNF nanocomposite, its Warburg line is positioned closer to the y-axis, indicating the presence of abundant conduits that enhance the transport of redox species. In stark contrast, the bare GCE exhibits poor transportation, evident from the substantial distance of its Warburg line from the *y*-axis.

These two parameters collectively emphasize the catalytic improvements achieved through the modification of the GCE with $NdNbO_4$/f-CNF, revealing it as an electrocatalyst with enhanced capabilities for promoting fast and efficient electron mobilization in electrochemical processes.

Furthermore, the electrochemical characteristics of the GCE with various modifications were studied through CV in the same redox probe (5 mM $Fe(CN)_6^{4-}/Fe(CN)_6^{3-}$ in 1 M KCl). Fig. S2† presents the CV profiles, featuring distinct redox peaks for the unmodified GCE, $NdNbO_4$/GCE, f-CNF/GCE, and $NdNbO_4$/f-CNF/GCE. The CV profile of the bare GCE revealed a suppressed redox peak current accompanied by a broad peak-to-peak separation, indicative of limited electron mobility at the electrode–electrolyte interface. The introduction of modifications, either with pure $NdNbO_4$ or f-CNF, resulted in a substantial augmentation of peak current and a reduction in peak-to-peak separation. These enhancements are attributed to the highly responsive electrode processes occurring in the interlayer region. Notably, $NdNbO_4$/f-CNF/GCE exhibited an extraordinary redox peak current with a minor peak-to-peak separation, highlighting the synergistic electrochemical advantages derived from the individual constituents within the nanocomposite. Fig. S3(A)† depicts the electrode's response to increasing scan rates, showing a consistent rise in peak current and distinct divergence in the potential. The relationship between the redox current and the square root of the scan rate was then plotted (Fig. S3(B)†), revealing a proportional correlation. The kinetics of the reversible reaction were characterized by regression equations for the anodic and cathodic scans, denoted as I_{pa} (μA) = 538.99 $\upsilon^{1/2}$ (mV s^{-1}) − 0.6018 and I_{pc} (μA) = −474.84 $\upsilon^{1/2}$ (mV s^{-1}) − 7.3577, respectively, with high regression coefficients of 0.9998 and 0.9996. To quantify the electrochemically active surface area of the fabricated sensor, eqn (3) was employed and the obtained EASA value for

$NdNbO_4$/f-CNF/GCE was found to be 1.45 cm^2. The augmented electroactive surface proves advantageous for the electrocatalytic activity of the engineered electrode, facilitating improved electrolyte penetration.

3.3. Optimization of the sensing platform

3.3.1. Effect of electrode modification. The impact of different electrode modifications on the electrochemical characteristics was systematically investigated by comparing the fabricated electrodes to the unmodified GCE. This analysis aimed to comprehend the thermodynamic feasibility and kinetics of electron transfer reactions occurring at the electrode–electrolyte interface. Fig. 4(A) shows the voltammetry signals of vanillin, utilizing both bare and modified electrodes, with a scan rate of 50 mV s^{-1} and 0.1 M PBS as the supporting electrolyte. Examining the anodic peak current (Ipa) of the various electrodes reveals a distinctive hierarchy: bare GCE (2.25 μA) < $NdNbO_4$/GCE (2.34 μA) < f-CNF/GCE (3.27 μA) < $NdNbO_4$/f-CNF/GCE (5.98 μA), as depicted in Fig. 4(B). Conversely, the anodic peak potentials (E_{pa}) exhibit an inverse trend among the electrodes, as shown in Fig. 4(C). The unmodified GCE displays the weakest anodic response at 0.66 V, signifying the deprived electrooxidation of vanillin at the electrode surface due to the absence of electronic support from modifiers. $NdNbO_4$/GCE shows a slight improvement (0.65 V), attributed to the effective adhesion of $NdNbO_4$ to the printed carbon coating, thereby enhancing active sites for vanillin interaction. In f-CNF/GCE, the peak potential notably shifts to 0.62 V,

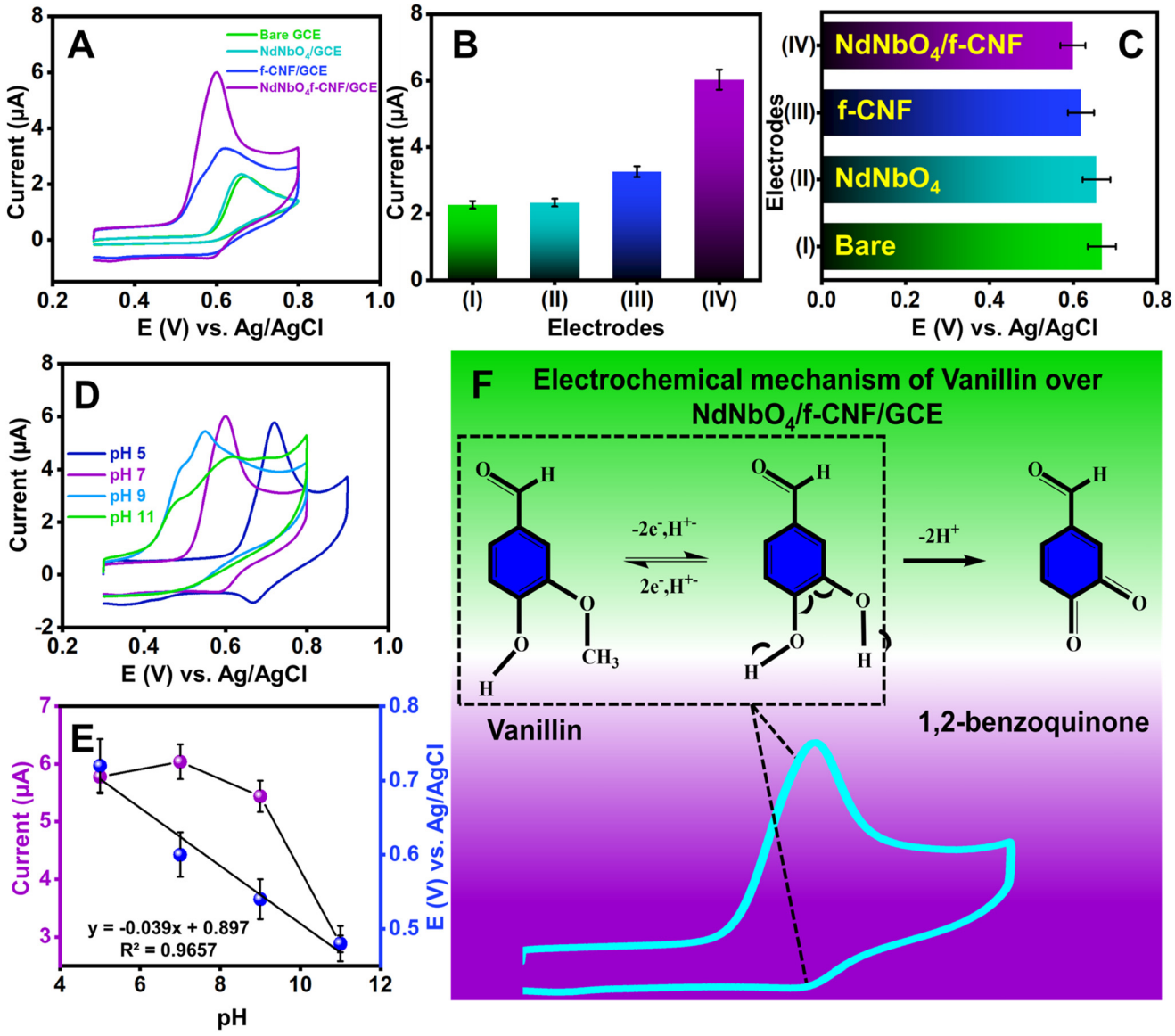

Fig. 4 (A) CV profiles of bare and modified electrodes with the addition of 100 μmol L^{-1} VAN; (B) histograms of modified electrodes as a function of peak current; (C) histograms of modified electrodes as a function of peak potential; (D) CV profile of $NdNbO_4$/f-CNF/GCE at different electrolyte pH values; (E) pH as a function of peak current and peak potential; and (F) electrochemical mechanism of VAN at $NdNbO_4$/f-CNF/GCE. All the experiments were conducted in 0.1 M PB and scanned at 50 mV s^{-1}.

attributed to the interaction between the aromaticity of the graphitic skeleton and the aromatic ring of vanillin moieties, enabling intense anodic peaks through π electron delocalization. The CV profile of $NdNbO_4$/f-CNF/GCE demonstrates a robust affinity toward vanillin, attributed to the synergistic effect and quantum confinement facilitated by the hybrid heterojunction. The nanocomposite establishes strong interactions with vanillin, forming hydrogen bonds with functional groups and interacting with electronegative groups, especially double bonds with π electrons, thereby amplifying the signal at a more negative potential (0.59 V).

3.3.2. Effect of pH. The pH of the supporting electrolyte is another significant factor influencing the amplification of CV signals. Fig. 4(D) illustrates the CV profile of $NdNbO_4$/f-CNF/GCE obtained at different pH values of PBS from 5 to 11 through the addition of 100 μmol L^{-1} vanillin. Under acidic conditions (pH 5), the concentration of protons (H^+) is higher, and the increased ionic strength can affect the diffusion rates of vanillin involved in the redox reactions. This altered ion mobility can result in reduced mass transport to the electrode surface, impacting the observed CV response. Similarly, on moving to more basic conditions (pH 9 and 11), the presence of hydroxide ions (OH^-) can compete with other ions participating in the electrochemical reactions. This competition can affect the kinetics of the redox processes and lead to a reduction in current response, whereas neutral pH provides a balance in the concentration of H^+ and OH^- in the electrolyte. This balance is conducive to efficient ion mobility, facilitating the transport of redox species to and from the electrode surface during electrochemical reactions. The surface charge of the electrode is generally more stable and controllable at neutral pH. This stability ensures consistent adsorption and desorption of species on the electrode surface, contributing to reliable and reproducible electrochemical measurements. Conducting electrochemical studies under neutral conditions allows for a closer representation of physiological environments, facilitating the study of real sample matrices. Furthermore, the Nernst equation considers the involvement of H^+ in the cell reaction, evidencing the dependence of the peak potential of the reactions on the pH value. If the electrochemical process involves (m) the number of protons and (n) the number of electrode electrons,

$$A + mH^+ + ne^- \leftrightarrow B \quad (7)$$

The Nernst equation for the aforementioned process can be written as given below in eqn (8):

$$\frac{dE_{pa}}{dpH} = \frac{(-2.303\, mRT)}{nF} \quad (8)$$

Fig. 4(E) supports the proportionality between the peak potential and the pH of the electrolyte, as indicated by the regression equation I_{pa} (μA) = −0.039 (X) + 0.897 (R^2 = 0. 965). The slope of the linear model is used to estimate the m/n ratio. For this vanillin sensor, the m/n ratio was calculated to be approximately 1, indicating equivalent protons and electrons transfer.

3.3.3. Electrochemical mechanism of vanillin. The cyclic voltammograms of vanillin exhibit distinctive features during CV measurements. Specifically, on the forward scan, an anodic peak is observed, signifying a two-electron and one-proton loss ($-2e^-/-H^+$). Subsequently, during the reverse sweep, a separate cathodic peak emerges, accompanied by its corresponding oxidation peak in the subsequent cycle. This phenomenon is attributed to the formation of the 1,2-benzoquinone unit from concomitant oxidation of its catechol-based product, both arising from the hydrolysis of the 2-methoxy group in vanillin (Fig. 4(F)). It is noteworthy that the reduction behavior of vanillin has received comparatively limited attention in the literature. However, a few reports have delved into this aspect, revealing intriguing findings. For instance, in dimethylformamide, the reduction of vanillin has been associated with the generation of a dimer. Similarly, in aqueous solutions, an alternative reduction pathway leads to the formation of vanillyl alcohol.

3.3.4. Effect of vanillin concentration. Fig. 5(A) illustrates the apparent sensing capability of $NdNbO_4$/f-CNF/GCE in response to the sequential elevation in vanillin concentration in 0.1 M phosphate buffer at a scan rate of 0.05 V s^{-1}. The augmentation of vanillin concentration in the electrolyte from 50 to 250 μmol L^{-1} corresponds to an increase in the oxidative peak currents. This successive rise in current response is ascribed to the higher conductivity of the modified electrode induced by the quantum confinement of the nanocomposite. This confinement mechanism reduces the charge transportation barrier at the electrified interface, facilitating the oxidation of vanillin. Consequently, each incremental addition of vanillin results in anodic currents, contributing to the overall current response. The inherent structure of vanillin further promotes signal amplification due to its aromaticity and functionalities involved in π–π interactions. Additionally, there are hydrogen bonding interactions with the modifier components, fostering a stable interaction with antifouling properties. The uniformity observed in the current upsurge concerning increasing concentration is graphically represented as a linear model in Fig. 5(B). The regression equation for the anodic peak current (I_{pa}) is given by I_{pa} (μA) = 0.0159 [VAN] − 3.111, with [VAN] denoting the vanillin concentration in μmol L^{-1}. The regression coefficient is reported as 0.9874 for I_{pa}.

3.3.5. Effect of $NdNbO_4$/f-CNF loading amount. The kinetics of the electrode process and the sensitivity in measuring vanillin were effectively governed by the optimal loading of the electrode modifier on the glassy carbon electrode (GCE). The impact of varying the volume of the $NdNbO_4$/f-CNF nanocomposite for electrode modification was investigated through the cyclic voltammetry (CV) profile depicted in Fig. 5(C). As the loading amount increases from 2 mg μL^{-1} to 8 mg μL^{-1}, the oxidative current response steadily rises up to 6 mg μL^{-1}. However, the current response diminishes upon further loading to 8 mg μL^{-1}. This observed behavior is influenced by the thickness of the coating and the passivation effect. A very

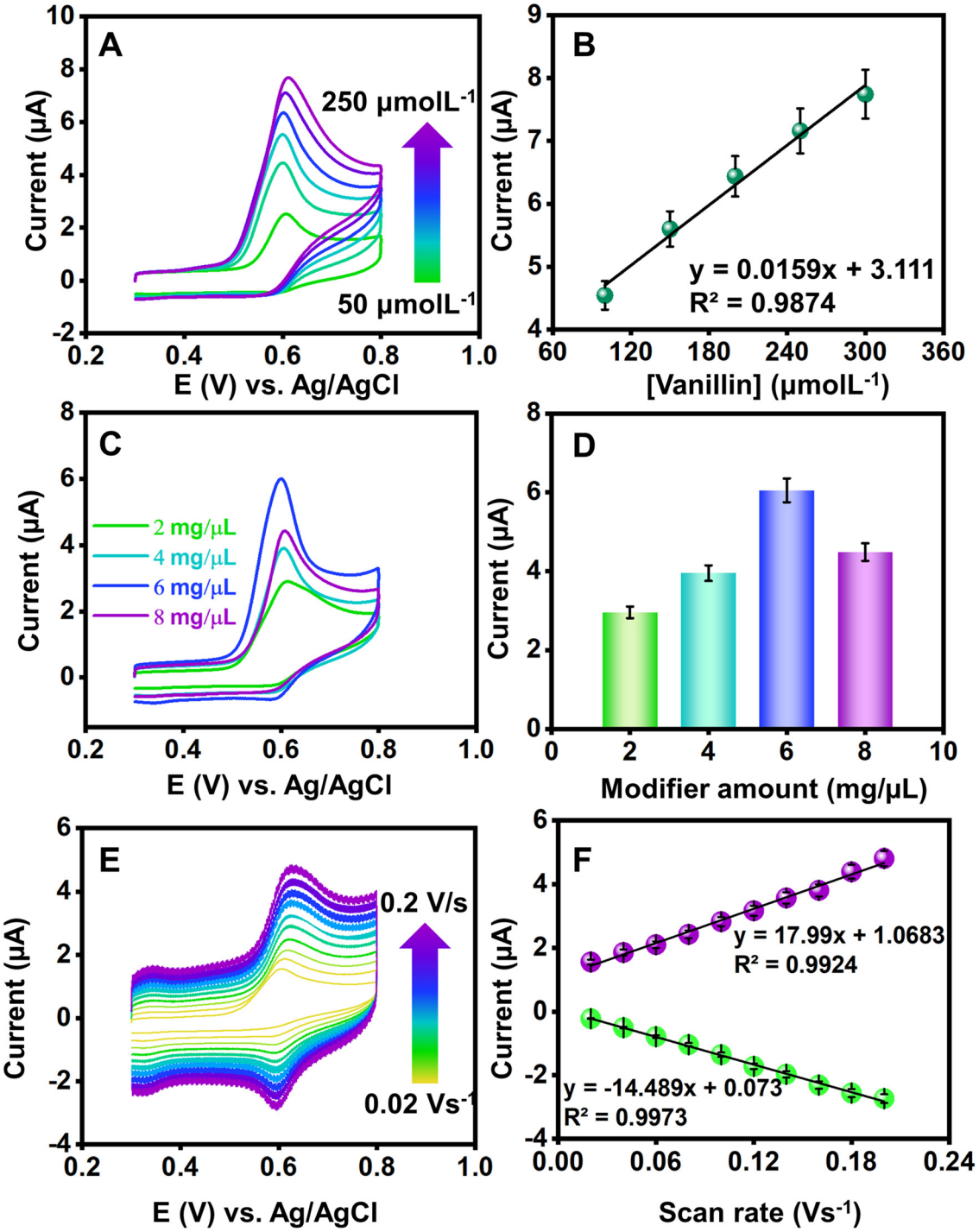

Fig. 5 (A) CV profile of $NdNbO_4$/f-CNF/GCE for increasing concentrations of VAN (50–250 μmol L^{-1}); (B) calibration plot of VAN concentration *versus* anodic peak current; (C) CV profile obtained for different loading amounts of the $NdNbO_4$/f-CNF nanocomposite over the GCE;(D) plot of loading amount *versus* anodic peak currents; (E) CV profile of 100 μmol L^{-1} VAN for varying scan rates from 0.02 to 0.2 V s^{-1}; and (F) calibration plot of increasing scan rates *versus* redox peak currents.

thin coating results in poor adsorption of the target analyte, leading to inadequate signal amplification with lower current values. Gradual increments in the volume of $NdNbO_4$/f-CNF lead to a higher thickness of the modifier film on the GCE. This facilitates solute penetration to the active core, promoting dynamic interactions between the fabricated electrode and vanillin molecules, resulting in improved current responses. However, with a further increase in the coating thickness, the electrode reaches saturation, hindering the passage of ions across the glassy carbon layer and the coated $NdNbO_4$/f-CNF

layer. Consequently, this impedes the detection of vanillin signals. The observed trend of the current response at different loading amounts is illustrated in Fig. 5(D). Therefore, a loading amount of 6 mg μL^{-1} for the modifier consistently fabricates the electrode in all experiments, striking a balance between the signal enhancement and the prevention of electrode saturation.

3.3.6. Effect of scan rate. A comprehensive understanding of the electrode kinetics governing the determination of menadione using $NdNbO_4$/f-CNF/GCE was achieved through cyclic voltammetry (CV), wherein scan rates were varied from 0.01 to 0.2 V s^{-1} in 0.1 M phosphate buffer. The redox peak currents exhibit a proportional increase with the scan rate, as illustrated in Fig. 5(E). Elevating the scan rates enhances electron transportation within the electrode, activating the electrocatalysts to initiate the reversible reaction of vanillin to 1,2-benzoquinone. The linear dependence of the scan rate on the redox peak currents was plotted according to the linear regression model (LRM), as shown in Fig. 5(F). The linearity coefficient is determined to be 0.9983, and the regression equation is expressed as I_{pa} (μA) = 0.2541 (V s^{-1}) − 0.0315 and I_{pa} (μA) = 0.2541 (V s^{-1}) − 0.0315. This calibration plot indicates that the electrode undergoes surface-controlled kinetics, further corroborated by the absence of a steady shift in peak potential. To authenticate the adsorption kinetics of the modified electrode, a -log plot of scan rate *versus* current was generated (Fig. S4†). The measured slope values, greater than 0.5 and closer to 1, align well with the theoretical value for a surface-controlled process, as proposed by the Laviron theory.

$$E_{pa} = E^{\circ} + \frac{RT}{\alpha nF}\ln\left(\frac{RTk_s}{\alpha nF}\right) + \frac{RT}{\alpha nF}\ln\,\vartheta \quad (9)$$

$$E_{pa} = E^{\circ} + \frac{RT}{(1-\alpha)nF}\ln\left(\frac{RTk_s}{(1-\alpha)nF}\right) - \frac{RT}{(1-\alpha)nF}\ln\,\vartheta \quad (10)$$

In the context of Laviron theory, the apparent charge transfer rate constant (k_s) and the charge transfer coefficient (α) of a surface-confined redox couple can be evaluated using the variation of anodic and cathodic peak potentials as a function of the logarithm of the scan rate (eqn (9) and (10)). The obtained value of α is 0.6115, within the theoretical range of 0.3–0.7, allowing the determination of n as 2, consistent with previous findings. Further investigation into electrode activity involves plotting redox peak currents *versus* the square root of the scan rate, as shown in Fig. S5.† This analysis reveals that the electrode is primarily governed by surface-controlled kinetics at lower scan rates. However, at higher scan rates, charge carriers diffuse into the active layers of the electrode, leading to amplified signals. Consequently, it is elucidated that reactions occurring at $NdNbO_4$/f-CNF/GCE depend on both diffusion and adsorption of vanillin towards the electrode. Additionally, a slight positive shift in the anodic peak and a slightly negative shift in the cathodic peak are observed.

3.4. Electrochemical detection of vanillin at $NdNbO_4$/f-CNF/GCE

DPV, a potentiodynamic method, involves applying potential pulses along with a linear ramp potential, dependent on the analyte concentration. In the analysis, qualitative insights into vanillin are gleaned from the half-wave potential ($E_{1/2}$). The DPV plot illustrates measured currents against applied potentials. Fig. 6(A) presents the DPV profile of $NdNbO_4$/f-CNF/GCE, revealing variations with increasing vanillin concentrations. Due to vanillin's organic nature, its adsorption on the electrode surface produces enhanced current responses, minimizing the capacitive current.

Optimizing DPV parameters led to a gradual peak current increase with increasing vanillin concentration, attributed to the sensor's antifouling properties. Linear regression demonstrated a proportional relationship between the measured current and the vanillin concentration, resulting in a regression equation: I_{pa} = 0.1601 [μmol L^{-1}] + 0.8621 (R^2 = 0.979) (Fig. 6(B)). The limit of detection (LOD) and the limit of quantification (LOQ) were determined using eqn (2) and (3).

Here, SD is the standard deviation of three blank signals and m is the regression model's slope. The fabricated sensor exhibited LOD and LOQ values of 6.3 and 21 nmol L^{-1}, respectively. The sensor's linearity spanned from 0.001 to 63.101 μmol L^{-1} and sensitivity within linear ranges was found to be 2.3 μA μ(μmol L^{-1})$^{-1}$ cm^{-2}. All the optimized parameters of the proposed sensor have been compared with the existing reports in the literature, as mentioned in Table 1, and found that the superiority of the fabricated sensor is mainly attributed to the synchronously activated hybrid heterojunction and quantum confinement of the nanocomposite modifying traditional electrodes.

3.5. Interference and precision studies

To investigate the potential impact of systematic errors originating from overlapping agents, DPV experiments were extended (Fig. 6(C)). Fig. 6(D) illustrates the relative error percentages in the current attributed to interferents like mercury ions, ascorbic acid, tertiary butyl hydroquinone, Trolox, theophylline, diethofencarb, and dopamine during vanillin sensing. Dopamine, a biomolecule, exerted maximum influence on current responses, while a food additive, vitamin and pesticides demonstrated a milder interference. The observed augmentation in the CV response was ascribed to the oxidative environment facilitating the mid-oxidation of functional groups attached to interfering moieties. However, it is crucial to note that the interference remains negligible and does not compromise the proposed sensor's performance. The precision of the fabricated sensor was assessed through CV experiments involving three distinct GCEs. Each GCE underwent identical modification employing the drop-casting method with a uniform amount of the $NdNbO_4$/f-CNF nanocomposite. The CV profiles of the $NdNbO_4$/f-CNF/GCE and the corresponding plot, which illustrates the relationship between the different GCEs and their relative current responses, are

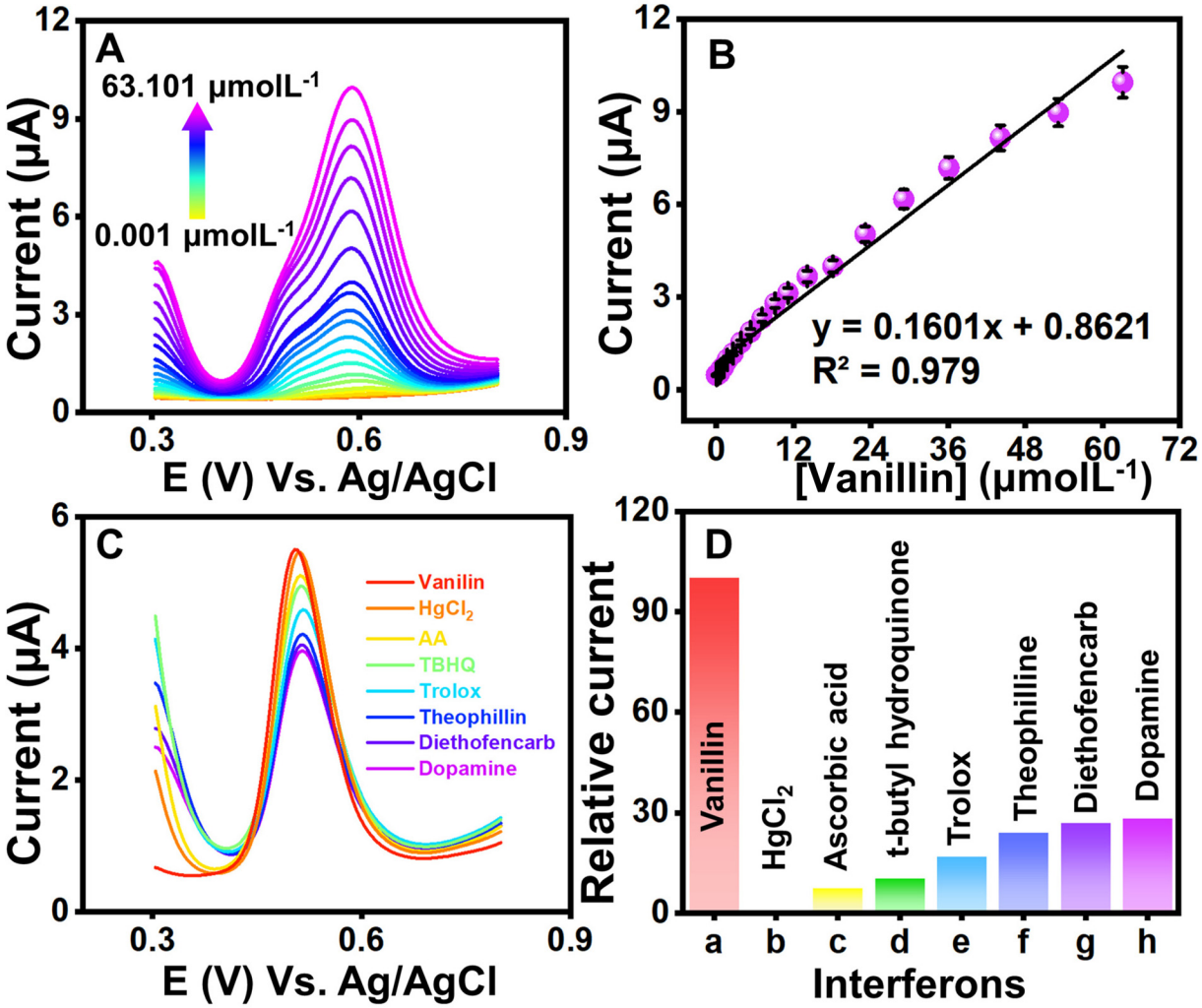

Fig. 6 (A) DPV curves obtained using $NdNbO_4$/f-CNF/GCE with a sequential increase in the VAN concentration; (B) corresponding linear dependence plot of VAN concentration *versus* anodic peak currents; (C) DPV profile for 100 μmol L^{-1} VAN at $NdNbO_4$/f-CNF/GCE in the presence of overlapping agents at the anodic scan; and (D) relative current error percentage obtained by each interferon with respect to the anodic peak current of VAN.

depicted in Fig. S6(A and B)† This comparative analysis highlights the variations in the current generated by each GCE, providing insight into the influence of the electrode composition and surface characteristics on the overall electrochemical activity of the $NdNbO_4$/f-CNF/GCE composite. To quantify precision, the relative standard deviation (RSD) was calculated using eqn (1). For the proposed sensor, the calculated RSD was 1.519%, falling below the accepted error threshold, indicating the reproducibility of the sensor. The CV profile in Fig. S9(A)† was obtained by performing repeated measurements four times using the $NdNbO_4$/f-CNF/GCE composite electrode. The corresponding plot in Fig. S7(B)† illustrates the relationship between these repetitive measurements and the observed current values. This analysis showcases the consistency of the electrode's electrochemical response. An RSD of 4.72% indicates a high degree of precision across the repeated measurements, underscoring the reliability of the $NdNbO_4$/f-CNF/GCE composite in maintaining consistent electrochemical performance. Extensive cycling was conducted to thoroughly assess the durability and electrochemical stability of the composite electrode under continuous operation. The resulting CV profiles in Fig. S8† demonstrate the electrode's ability to maintain consistent current responses throughout the 100 cycles, reflecting its robustness and long-term stability. This indicates that the $NdNbO_4$/f-CNF/GCE composite can reliably function in sensing applications without significant degradation in the performance over multiple uses.

3.6. Real sample analysis

Extending on the DPV investigations, an in-depth exploration was conducted to assess the viability of the established electrochemical sensor crafted from $NdNbO_4$/f-CNF/GCE for varying concentrations of vanillin in both milk chocolate and milk shake samples. The meticulously prepared sample underwent

Table 1 Comparative study of $NdNbO_4$/f-CNF-modified GCE's performance with existing electrodes in the literature

Fabricated electrode	Method of detection	Linearity range (μM)	LOD (μM)	Real samples	Ref.
ZnCr-LDH@g-CN/GCE[a]	DPV	0.001–143.2	0.009	Ice cream and chocolate	45
AuNPs/GR/GCE[b]	DPV	5–120	1.7	Cookies	46
FePc MOF/GCE[c]	DPV	0.22–29.14	0.05	Tablet and human serum	6
PMOMGPE[d]	DPV	10.0–35.0	0.073	Vanilla essence	47
f-MWCNTs-FNTs/CPE[e]	CV	0.05–9.0	0.034	Vanilla sugar	8
PTY/OL/CNPE[f]	DPV	2.0–40.0	0.049	Biscuits	48
MoS_2-CNF/GCE[g]	Amperometry	0.3 to 135	0.15	Cookie	1
Poly(GA)/(MWCNTs-GT)CPS[h]	DPV	0.50–13.0	0.019	Milkshake; cream cake; biscuit; vanilla extract.	49
CuO@SiO_2-modified electrode	DPV	0.05–1.2; 6.2–111.2	0.053	Biscuits and chocolates	50
La_2NiO_4@CNF/GCE[i]	DPV	0.005–235; 235–3035	0.0061	Chocolate; ice cream	22
MoS_2/PANI/f-CNTs[j]	DPV	3.6–125	0.021	Vanillin biscuit	51
MoS2/PANI@GO[k]	DPV	6–86.6	0.043	Commercial food and beverage samples	52
$NdNbO_4$/f-CNF/GCE	DPV	0.001 to 63.101	0.0063	Milk chocolate and milkshake	This work

[a] ZnCr-layered double hydroxide and g-CN. [b] Graphene (GR) decorated with gold nanoparticles (AuNPs). [c] Iron phthalocyanine (FePc)-based metal–organic framework. [d] Poly methyl orange-modified graphene. [e] Fullerenes (FNTs) and functionalized multi-walled carbon nanotubes (f-MWCNTs). [f] Poly (titan yellow) and octoxynol-9-modified carbon nanotube paste electrode. [g] Molybdenum disulfide (MoS_2) nanoparticle-decorated carbon nanofibers (MoS_2-CNFs). [h] Poly(glutamic acid)/multi-walled carbon nanotube–graphite composite. [i] Lanthanum nickelate spheres embedded acid functionalized carbon nanofiber composite. [j] Molybdenum disulfide/polyaniline/functionalized multi-walled carbon nanotubes. [k] Polyaniline blended molybdenum sulfide-decorated graphene oxide.

dilution with PBS, serving as the supporting electrolyte, wherein a sequential addition of vanillin was systematically performed. The analytical performance of the developed sensor within a real sample matrix was investigated for increasing concentrations of vanillin ranging from 50 to 250 μM, as illustrated in Fig. S9 and S10.† Utilizing the LRM, the correlation between the peak current and the concentration was elucidated through an equivalent plot, as shown in the inset of Fig. S9 and S10.†

The LOD, calculated employing the standard deviation method for the electrochemical sensing of vanillin using $NdNbO_4$/f-CNF/GCE, was determined to be 7.59 and 9.38 nmol L^{-1} in milk chocolate and milk shake samples. Consequently, the fabricated DPV sensor adeptly transforms the oxidation of vanillin on the surface of the $NdNbO_4$/f-CNF-modified GCE into discernible signals in the form of peak current. This mechanism effectively quantifies the target analyte within the complex food sample matrix, confirming the sensor's efficacy in real-world applications.

4. Conclusion

This research underscores the application of a hydrothermal approach to synthesize nano-spheres of $NdNbO_4$, which are then incorporated with f-CNF *via* sonication, culminating in a nanocomposite serving as an electrode modifier, maintaining its structural integrity. A comprehensive array of analytical methods, including XRD, Raman, FTIR, SEM, and TEM, was employed to investigate the improved characteristics resulting from the synergistic interactions among the counterparts of the nanocomposite. Voltammetry and impedance experiments unveiled that the $NdNbO_4$/f-CNF-modified GCE manifested commendable electrocatalytic activity, enhancing electron transfer and furnishing enhanced reaction sites accessible to vanillin. The modified electrode exhibited notable electrochemical stability, resistance to fouling, low electrode/electrolyte impedance, and a substantial surface area. Evaluation encompassing LOD, selectivity, sensitivity, stability, reproducibility, and repeatability corroborated the sensing ability. Crucially, the practical utility of the developed sensor was validated through the successful detection of vanillin in food matrices, showcasing remarkable recovery rates. The fabrication of such sophisticated architectures, characterized by minimal energy consumption and negligible by-products, positions them as promising contenders for a diverse array of future applications.

Conflicts of interest

The authors declare no conflicts of interest in this research work.

Acknowledgements

This work was supported by the Ministry of Science and Technology (Special Research Project-MOST-108-2221-E-027-063).

References

1 M. Qianwen, D. Yaping, L. Li, W. Anqing, D. Dingding and Z. Yijun, *J. Electroanal. Chem.*, 2019, **833**, 297–303.
2 N. J. Walton, M. J. Mayer and A. Narbad, *Phytochemistry*, 2003, **63**, 505–515.
3 K. Murtada and V. Moreno, *J. Electroanal. Chem.*, 2020, **861**, 113988.

4 D. Zheng, C. Hu, T. Gan, X. Dang and S. Hu, *Sens. Actuators, B*, 2010, **148**, 247–252.
5 Y. Sun, X. Jiang, H. Jin and R. Gui, *Anal. Chim. Acta*, 2019, **1083**, 101–109.
6 J. Peng, L. Wei, Y. Liu, W. Zhuge, Q. Huang, W. Huang, G. Xiang and C. Zhang, *RSC Adv.*, 2020, **10**, 36828–36835.
7 C. I. Fort, S. C. A. Cobzac and G. L. Turdean, *Food Chem.*, 2022, **385**, 132711.
8 L. Taouri, M. Bourouina, S. Bourouina-Bacha and D. Hauchard, *J. Food Compos. Anal.*, 2021, **100**, 103811.
9 M. Perini, S. Pianezze, L. Strojnik and F. Camin, *J. Chromatogr., A*, 2019, **1595**, 168–173.
10 Z. Wang, G. Zeng, X. Wei, B. Ding, C. Huang and B. Xu, *Food Anal. Methods*, 2016, **9**, 3360–3366.
11 S. S. Hingse, S. B. Digole and U. S. Annapure, *J. Anal. Sci. Technol.*, 2014, **5**, 1–9.
12 M. Takahashi, S. Sakamaki and A. Fujita, *Biosci., Biotechnol., Biochem.*, 2013, **77**, 595–600.
13 Y. Shen, C. Han, B. Liu, Z. Lin, X. Zhou, C. Wang and Z. Zhu, *J. Dairy Sci.*, 2014, **97**, 679–686.
14 H. Duan, X. Li, L. Li, X. Wang, J. Feng, M. Sun and C. Luo, *Anal. Methods*, 2014, **6**, 8706–8712.
15 M. Ohashi, H. Omae, M. Hashida, Y. Sowa and S. Imai, *J. Chromatogr., A*, 2007, **1138**, 262–267.
16 O. Folin and W. Denis, *Ind. Eng. Chem.*, 1912, **4**, 670–672.
17 I. J. D. Priscillal and S.-F. Wang, *Nanoscale*, 2023, **15**, 8693–8705.
18 E. Bakker and M. Telting-Diaz, *Anal. Chem.*, 2002, **74**, 2781–2800.
19 B. J. Privett, J. H. Shin and M. H. Schoenfisch, *Anal. Chem.*, 2010, **82**, 4723–4741.
20 I. Baranowska, P. Markowski, A. Gerle and J. Baranowski, *Bioelectrochemistry*, 2008, **73**, 5–10.
21 G. Pierini, S. Robledo, J. López, A. Tesio, H. Fernández, A. Granero and M. Zon, *J. Mach. Form. Technol.*, 2018, **10**, 15–49.
22 E. J. Nixon, R. Sakthivel, Z. A. Alothman, P. S. Ganesh and R.-J. Chung, *Food Chem.*, 2023, **409**, 135324.
23 S.-Z. Shah, I. H. Taqvi, S. Ameen, A. Mallah, J. A. Buledi, N. H. Khand and A. R. Solangi, *Pure and Applied Chemistry*, 2023.
24 R. Nehru, C.-W. Chen and C.-D. Dong, *Carbon*, 2023, **208**, 410–420.
25 S. Vinoth and S.-F. Wang, *New J. Chem.*, 2023, **47**, 9229–9238.
26 J. Huang, Y. Liu and T. You, *Anal. Methods*, 2010, **2**, 202–211.
27 J. Singh, A. Roychoudhury, M. Srivastava, P. R. Solanki, D. W. Lee, S. H. Lee and B. Malhotra, *J. Mater. Chem. B*, 2013, **1**, 4493–4503.
28 P. Sarin, R. W. Hughes, D. R. Lowry, Z. D. Apostolov and W. M. Kriven, *J. Am. Ceram. Soc.*, 2014, **97**, 3307–3319.
29 L. Brixner, J. Whitney, F. Zumsteg and G. Jones, *Mater. Res. Bull.*, 1977, **12**, 17–24.
30 K. Byrappa and T. Adschiri, *Prog. Cryst. Growth Charact. Mater.*, 2007, **53**, 117–166.
31 H. Zhao, S. Feng, W. Xu, Y. Shi, Y. Mao and X. Zhu, *J. Mater. Chem.*, 2000, **10**, 965–968.
32 G. Blasse and A. Corsmit, *J. Solid State Chem.*, 1973, **6**, 513–518.
33 Y. Repelin, E. Husson, F. Bennani and C. Proust, *J. Phys. Chem. Solids*, 1999, **60**, 819–825.
34 Q. Qiao, S. Singh, S.-L. Lo, Y. Li, J. Jin and L. Wang, *J. Taiwan Inst. Chem. Eng.*, 2018, **84**, 110–122.
35 T. Liu and H. Lei, *Appl. Surf. Sci.*, 2017, **413**, 16–26.
36 R. Chen, W. Wang, D. Jiang, X. Chu, X. Ma and Q. Zhan, *J. Phys. Chem. Solids*, 2018, **117**, 28–35.
37 P. Yu, W. Guo, T. Gao, L. Su and J. Xu, *Optik*, 2018, **162**, 102–107.
38 A. Lubenchenko, A. Batrakov, I. Shurkaeva, A. Pavolotsky, S. Krause, D. Ivanov and O. Lubenchenko, *J. Surf. Invest.: X-Ray, Synchrotron Neutron Tech.*, 2018, **12**, 692–700.
39 A. Dacca, G. Gemme, R. Parodi and L. Mattera, *Part. Accel.*, 1998, **60**, 103–120.
40 C. Morant, J. Andrey, P. Prieto, D. Mendiola, J. Sanz and E. Elizalde, *Phys. Status Solidi A*, 2006, **203**, 1069–1075.
41 B. M. Abu-Zied, *Appl. Surf. Sci.*, 2019, **471**, 246–255.
42 Y. Zhou, N. Wang, X. Qu, F. Huang, Y. Duan, X. Zhang, X. Dong and Z. Zhang, *Nanoscale*, 2019, **11**, 19994–20005.
43 I. J. Daisy Priscillal and S.-F. Wang, *ACS Appl. Nano Mater.*, 2022, **5**, 10331–10340.
44 I. J. D. Priscillal and S.-F. Wang, *Microchem. J.*, 2023, **187**, 108396.
45 S. Gopi and S.-F. Wang, *Microchim. Acta*, 2023, **190**, 423.
46 X. Si, M. Han, W. Li, C. Bai, X. Xu and J. Xu, *Curr. Anal. Chem.*, 2022, **18**, 818–825.
47 A. B. Monnappa, J. G. G. Manjunatha, A. S. Bhatt and H. Nagarajappa, *J. Sci.: Adv. Mater. Devices*, 2021, **6**, 415–424.
48 G. Tigari, J. Manjunatha, E. S. D'Souza and N. Sreeharsha, *ChemistrySelect*, 2021, **6**, 2700–2708.
49 N. Hareesha, J. Manjunatha, B. Amrutha, N. Sreeharsha, S. B. Asdaq and M. K. Anwer, *Colloids Surf., A*, 2021, **626**, 127042.
50 A. Venkadesh, J. Mathiyarasu and S. Radhakrishnan, *Mater. Today Chem.*, 2021, **22**, 100554.
51 E. Murugan and A. Dhamodharan, *Diamond Relat. Mater.*, 2022, **128**, 109268.
52 E. Murugan, A. Dhamodharan and S. Saranya, *Indian J. Chem. Technol.*, 2022, **28**, 518–527.